LIQUID CRYSTALS

Three-dimensional crystals of adaptive knots

Jung-Shen B. Tai[1] and Ivan I. Smalyukh[1,2,3]*

Starting with Gauss and Kelvin, knots in fields were postulated to behave like particles, but experimentally they were found only as transient features or required complex boundary conditions to exist and could not self-assemble into three-dimensional crystals. We introduce energetically stable, micrometer-sized knots in helical fields of chiral liquid crystals. While spatially localized and freely diffusing in all directions, they resemble colloidal particles and atoms, self-assembling into crystalline lattices with open and closed structures. These knots are robust and topologically distinct from the host medium, though they can be morphed and reconfigured by weak stimuli under conditions such as those in displays. A combination of energy-minimizing numerical modeling and optical imaging uncovers the internal structure and topology of individual helical field knots and the various hierarchical crystalline organizations that they form.

Topological order and phases represent an exciting frontier of modern research (*1*), but topology-related ideas have a long history in physics (*2*). Gauss postulated that knots in fields could behave like particles, whereas Kelvin, Tait, and Maxwell believed that matter, including crystals, could be made of real-space, free-standing knots of vortices (*2*–*4*). These early physics models, introduced long before the very existence of atoms was widely accepted, gave origins to modern mathematical knot theory (*2*–*4*). Expanding this topological paradigm, Skyrme and others modeled subatomic particles with different baryon numbers as nonsingular topological solitons and their clusters (*3*–*5*). Knotted fields emerged in classical and quantum field theories (*3*–*7*) and in scientific branches ranging from fluid mechanics to particle physics and cosmology (*2*–*11*). In condensed matter, arrays of singular vortex lines and low-dimensional analogs of Skyrme solitons were found as topologically nontrivial building blocks of exotic thermodynamic phases in superconductors, magnets, and liquid crystals (LCs) (*12*–*14*). Could they be knotted, and could these knots self-organize into three-dimensional (3D) crystals? Knotted fields in condensed matter found many experimental and theoretical embodiments, including both nonsingular solitons and knotted vortices (*7*–*9*, *15*–*23*). However, they were metastable and decayed with time (*7*–*9*, *15*–*17*) or could not be stabilized without colloidal inclusions (*18*, *19*) or confinement and boundary conditions (*20*–*22*), and could not self-organize into 3D lattices (*22*, *23*). We introduce energetically stable, micrometer-sized adaptive knots in chiral LCs that, unexpectedly, materialize the knotted vortices and nonsingular solitonic knots at the same time and indeed behave like particles, undergoing 3D Brownian motion and self-assembling into 3D crystals.

Helical fields, as in the familiar example of circularly polarized light with electric and magnetic fields periodically rotating around the Poynting vector, are ubiquitous in chiral materials such as magnets and LCs. These helical fields comprise a triad of orthonormal fields (Fig. 1A), namely the material alignment field $\boldsymbol{n}(\boldsymbol{r})$ (of rodlike molecules in LCs or spins in magnets) and the immaterial line fields along the helical axis $\boldsymbol{\chi}(\boldsymbol{r})$, analogous to the Poynting vector, and $\boldsymbol{\tau}(\boldsymbol{r})\perp\boldsymbol{n}(\boldsymbol{r})\perp\boldsymbol{\chi}(\boldsymbol{r})$. For LCs, $\boldsymbol{n}(\boldsymbol{r})$ is nonpolar but can be decorated with unit vector fields (*14*, *24*). The distance over which $\boldsymbol{n}(\boldsymbol{r})$ and $\boldsymbol{\tau}(\boldsymbol{r})$ rotate around $\boldsymbol{\chi}(\boldsymbol{r})$ by 2π within the helical structure is the helical pitch p (Fig. 1A). We demonstrate knotted fields that in $\boldsymbol{n}(\boldsymbol{r})$ are topological solitons with interlinked, closed-loop preimages resembling Hopf fibration (Fig. 1B). At the same time, the nonpolar nature of $\boldsymbol{\chi}(\boldsymbol{r})$ and $\boldsymbol{\tau}(\boldsymbol{r})$ permits the half-integer singular vortex lines to form various torus knots (Fig. 1C) while retaining the fully nonsingular nature of $\boldsymbol{n}(\boldsymbol{r})$. Therefore, our topological soliton in the helical field is a hybrid embodiment of both interlinked preimages and knotted vortex lines, which can be realized to have this solitonic nonsingular nature in systems with either polar or nonpolar $\boldsymbol{n}(\boldsymbol{r})$ (*12*–*14*). We find these knot solitons, which we call "heliknotons," embedded in a helical background and forming spontaneously after transition from the isotropic to LC phase when a weak electric field $\boldsymbol{E}$ is applied to a positive-dielectric-anisotropy chiral LC along the far-field helical axis $\boldsymbol{\chi}_0$. The materials used are prepared as mixtures LC-1 through LC-3 (*24*) of commercially available, room-temperature nematics and chiral dopants. In bulk LC samples of typical thickness within d = 10 to 100 μm (*24*), heliknotons display 3D particle–like properties and form a dilute gas at low number densities (Fig. 1D), with orientations of shape-anisotropic solitonic structures correlated with their positions along $\boldsymbol{\chi}_0$ (Fig. 1, D and E). Depending on materials and applied voltage U, heliknotons can adopt different shapes (Fig. 1, D to G), which are reproduced by numerical modeling (insets of Fig. 1, F and G) based on minimization of the free energy (*24*):

$$F = \int d^3\boldsymbol{r}\left\{\frac{K}{2}(\nabla\boldsymbol{n})^2 + \frac{2\pi K}{p}\boldsymbol{n}\cdot(\nabla\times\boldsymbol{n}) - \frac{\varepsilon_0\Delta\varepsilon}{2}(\boldsymbol{n}\cdot\boldsymbol{E})^2\right\} \quad (1)$$

where K is the average elastic constant, $\Delta\varepsilon$ is the LC's dielectric anisotropy, and ε_0 is the vacuum permittivity. The integrand comprises energy terms originating from elastic deformation, chirality, and dielectric coupling, respectively. Minimization of F at different U and $\Delta\varepsilon$ (table S1) reveals that heliknotons can be stable, metastable, or unstable with respect to the helical background (Fig. 1H), comprising localized regions (depicted in gray in Fig. 1, B and C) of perturbed helical fields and twisting rate.

Heliknotons undergo Brownian motions (Fig. 1I and movie S1) and exhibit anisotropic interactions while moving along $\boldsymbol{\chi}_0$ and in the lateral directions (Fig. 1, E and J, and movie S2) (*24*). The inter-heliknoton pair-interaction potential is anisotropic and highly tunable, from attractive to repulsive and from tens to thousands k_BT (where k_B is Boltzmann constant and T is temperature), depending on the choice of LC, U, and sample thickness (Fig. 1J). Similar to nematic colloids (*25*, *26*), interactions between localized heliknotons arise from sharing long-range perturbations of the helical fields around them and minimizing the overall free energy for different relative spatial positions of these solitons. These interactions lead to a plethora of crystals, including low-symmetry and open lattices that were recently achieved in colloids (*26*–*28*) (Fig. 2). In thin cells of thickness $d\lesssim 4p$, heliknotons localize around the sample's horizontal midplane, making their anisotropic interactions quasi-2D. Heliknotons self-assemble (movie S3) into a 2D rhombic lattice both when the attractive potential is ~1000 k_BT (Fig. 2, A and B) and when it is ~10 k_BT (Fig. 2, C and D). From initial positions defined by laser tweezers (*24*), heliknotons self-assemble into a stretched kagome lattice with anisotropic binding energies ~100 k_BT (Fig. 2E). Such open lattices have interesting topological properties (*28*), potentially bringing about an interplay between topologies of the crystal's basis and lattice. Crystallographic symmetries and lattice parameters can be controlled through tuning reconfigurable interactions, such as switching reversibly between synclinic and anticlinic tilting of heliknotons via changing U by <0.5 V (Fig. 2, F and G, and movie S4).

3D crystals of heliknotons emerge at $d > 4p$, when anisotropic interactions yield triclinic lattices (Fig. 2, H to N). One can watch initially

[1]Department of Physics, University of Colorado, Boulder, CO 80309, USA. [2]Materials Science and Engineering Program, Soft Materials Research Center, and Department of Electrical, Computer & Energy Engineering, University of Colorado, Boulder, CO 80309, USA. [3]Renewable and Sustainable Energy Institute, National Renewable Energy Laboratory and University of Colorado, Boulder, CO 80309, USA.
*Corresponding author. Email: ivan.smalyukh@colorado.edu

quasi-2D pre-self-assembled crystallites interacting with each other while moving in lateral and axial directions (Fig. 2, J to M, and movie S5), forming different crystallographic planes of the 3D triclinic lattice. The helical background LCs, individual heliknotons, and the ensuing lattices are all chiral. The lowest-symmetry triclinic pedial lattices can have primitive cells comprising two (Fig. 2, H and J to M, and movie S5) or three (Fig. 2, I and N, and movie S6) crystallographic planes, depending on relative orientations of heliknotons within these planes. The two lattices with parallel (Fig. 2M) and orthogonal (Fig. 2N) relative orientations of heliknotons in consecutive heliknoton layers are just examples as the angle between heliknotons within crystallographic planes along $\boldsymbol{\chi}_0$ can be tuned (Fig. 1E) by U, material, and geometric parameters. Because the heliknotons have anisometric shape (like LC molecules) and can exhibit spatial twists, hierarchical topological solitons comprising heliknotons could potentially emerge. Heliknoton crystals exhibit giant anisotropic electrostriction (Fig. 2O and movies S7 and S8). For example, upon changing from U = 3.0 to 4.4 V, one lattice parameter in the insets of Fig. 2O extends by ~44%, whereas the other only by ~4%. This electrostriction is consistent with the free-energy minimization (Fig. 2P) for 3D crystals of heliknotons with tunable lattice parameters at different U. The experimentally observed soliton crystals correspond to minima of free energy within a broad range of applied voltages (*24*), consistent with their facile self-organization into triclinic pedial crystals and other reconfigurable 3D and 2D lattices (Fig. 2). As the applied field is increased even further, the heliknoton crystals become metastable and then unstable with respect to the unwound state with $\boldsymbol{n}(\boldsymbol{r})||\boldsymbol{E}$ (*24*).

Numerical modeling and experiments reveal detailed structures of the fields within a heliknoton (*24*) (Fig. 3, A to I, and fig. S1). In $\boldsymbol{n}(\boldsymbol{r})$, the continuous localized configuration of a heliknoton is embedded in a helical background (Fig. 3, A to C) and has all closed-loop preimages linked with each other once, with the linking number +1 (Fig. 3J and fig. S1). Up to numerical precision, this matches the Hopf index calculated through numerical integration (*22*):

$$Q = \frac{1}{64\pi^2}\int d^3\boldsymbol{r}\epsilon^{ijk}A_iB_{jk} \qquad (2)$$

where $B_{ij} = \epsilon_{abc}n^a\partial_i n^b\partial_j n^c$, ϵ is the totally antisymmetric tensor, A_i is defined as $B_{ij} = (\partial_i A_j - \partial_j A_i)/2$, and the summation convention is assumed. Spatial structures of $\boldsymbol{\chi}(\boldsymbol{r})$ and $\boldsymbol{\tau}(\boldsymbol{r})$ are derived from the energy-minimizing $\boldsymbol{n}(\boldsymbol{r})$ using the eigenvector of the chirality tensor (*24*, *29*, *30*) (Fig. 3, D to I). They exhibit torus knots of spatially colocated singular half-integer vortices, within which $\boldsymbol{\chi}(\boldsymbol{r})$ and $\boldsymbol{\tau}(\boldsymbol{r})$ nonpolar fields rotate by 180° around the vortex line in the plane locally orthogonal to it (Fig. 3, D to I). The closed loop of the vortex line is the righthanded T(2,3) trefoil torus knot, also labeled as the 3_1 knot in the Alexander–Briggs notation (Fig. 3, K and L). The singular vortex knots in $\boldsymbol{\chi}(\boldsymbol{r})$ and $\boldsymbol{\tau}(\boldsymbol{r})$ also correspond to a colocated knot of a meron (topologically nontrivial structure of a fractional 2D skyrmion tube) in $\boldsymbol{n}(\boldsymbol{r})$ (fig. S2). Handedness of the knots and links matches that of chiral $\boldsymbol{n}(\boldsymbol{r})$, implying that the sign of Hopf indices of such energy-minimizing solitons is dictated by LC's chirality. Simulated and experimental depth-resolved nonlinear optical images of heliknotons for different polarizations of excitation light closely agree (Fig. 3, M to O), confirming experimental reconstruction of the field (*24*). Unlike the Shankar solitons (*11*), which exemplify condensed matter models with topology of a triad of orthonormal fields similar to that of Skyrme solitons in nuclear physics, heliknotons exhibit nonsingular structure only in one of the three fields, though they are still overall nonsingular in the material field. Differing from transient textures of linked loops of nonsingular disclinations (*15*, *16*) and metastable loops of singular vortices (*17*) in cholesteric LCs, our heliknotons are stable torus knots of colocated merons in $\boldsymbol{n}(\boldsymbol{r})$ and vortices in $\boldsymbol{\chi}(\boldsymbol{r})$ and $\boldsymbol{\tau}(\boldsymbol{r})$ that enable ground-state 3D crystals of knots (Fig. 2 and fig S2).

In addition to the $Q = 1$ heliknotons with equilibrium dimensions between p and $2p$, we also find larger $Q = 2$ topological solitons (Fig. 4A), for which experimental polarizing

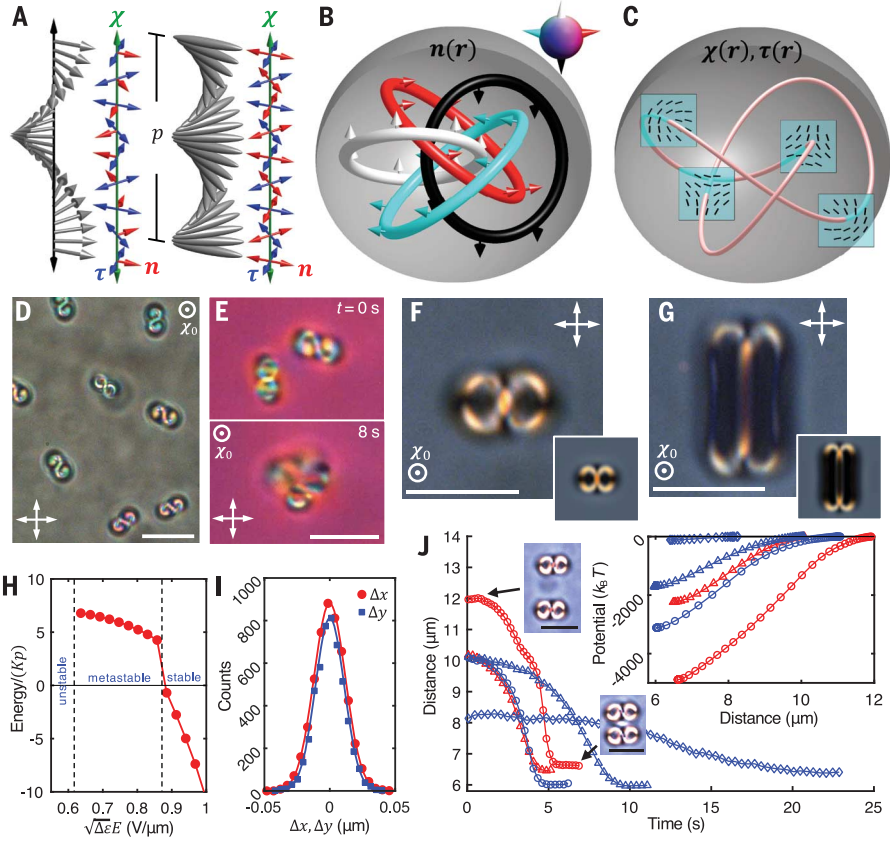

Fig. 1. Knots in helices. (**A**) Helical field comprising a triad of orthonormal fields $\boldsymbol{n}(\boldsymbol{r})$, $\boldsymbol{\chi}(\boldsymbol{r})$, and $\boldsymbol{\tau}(\boldsymbol{r})$, with $\boldsymbol{n}(\boldsymbol{r})$ being either polar (left) or nonpolar (right). (**B**) Preimages in $\boldsymbol{n}(\boldsymbol{r})$ of a heliknoton colored according to their orientations on $\mathbb{S}^2$ (top right inset). (**C**) Knotted colocated half-integer vortex lines in $\boldsymbol{\chi}(\boldsymbol{r})$ and $\boldsymbol{\tau}(\boldsymbol{r})$. In (B) and (C), the gray isosurfaces show regions of distorted helical background. (**D**) A gas of heliknotons in LC-1 sample of thickness 30 μm at U = 4.5 V. (**E**) Two heliknotons interact in 3D while forming a dimer in LC-2 sample of thickness 30 μm at U = 11.0 V. (**F** and **G**) Polarizing optical micrographs of metastable and stable heliknotons at U = 4.3 and 4.5 V, respectively, in a sample with $d = 10$ μm, with computer-simulated counterparts shown in the bottom right insets. (**H**) Free energy of individual heliknotons versus $\boldsymbol{E}$, where energy of the helical state equals zero; the helical state and heliknotons are unstable at $\sqrt{\Delta\varepsilon}E \gtrsim 1$V/μm when the field tends to align $\boldsymbol{n}(\boldsymbol{r})||\boldsymbol{E}$ (*24*). (**I**) Displacement histograms Δx and Δy showing diffusion of the heliknoton in (F) in orthogonal lateral directions perpendicular to $\boldsymbol{\chi}_0$. Experimental and numerical data were obtained for LC-1 in (D) and LC-2 in (E) to (I). (**J**) Pair interaction of heliknotons. Data shown in red (at voltages ○, 4.2 V; △, 2.9 V) were obtained for LC-2 and those in blue (○, 1.4 V; △, 1.0 V; ◇, 1.7 V) for LC-1 at $d = 10$ μm (*24*). Scale bars indicate 10 μm and $p = 5$ μm.

micrographs also match their numerical counterparts. A $Q = 2$ heliknoton contains a larger region of distorted helical background in both the lateral and axial directions (Fig. 4, A to D, and figs. S3 and S4). Preimages for two antiparallel vertical orientations of $\boldsymbol{n}(\boldsymbol{r})$ form a pair of Hopf links (Fig. 4H), linked twice, like all other preimage pairs. Singular vortex lines in $\boldsymbol{\chi}(\boldsymbol{r})$ and $\boldsymbol{\tau}(\boldsymbol{r})$ form closed cinquefoil T(2,5) torus knots (also labeled as 5_1 knots) colocated with a similar knot of a meron tube in $\boldsymbol{n}(\boldsymbol{r})$. A $Q = 3$ heliknoton contains three Hopf links of preimages with a net linking number of 3 for each preimage pair (Fig. 4I and figs. S5 and S6). The singular vortex lines in $\boldsymbol{\chi}(\boldsymbol{r})$ and $\boldsymbol{\tau}(\boldsymbol{r})$ form a T(2,7) torus knot (the 7_1 knot), colocated with the same knot of a meron tube in $\boldsymbol{n}(\boldsymbol{r})$ (Fig. 4, E, F, and I). Figure 4, G to I, shows both preimages of the antiparallel vertical orientations of $\boldsymbol{n}(\boldsymbol{r})$ and vortex lines in $\boldsymbol{\chi}(\boldsymbol{r})$ and $\boldsymbol{\tau}(\boldsymbol{r})$, as well as the Reidemeister moves simplifying their structures. Topologically disinct heliknotons have different numbers of crossings in the free-standing knots of vortex lines and different linking of preimages, which were key topological invariants in early models of atoms and subatomic particles (*2*–*6*). For different heliknotons, Q is related to crossing number N of the vortex knots: $N = 2Q + 1$. The closed loop of preimages in $\boldsymbol{n}(\boldsymbol{r})$ are interlinked with the torus knots of vortices in $\boldsymbol{\chi}(\boldsymbol{r})$ and $\boldsymbol{\tau}(\boldsymbol{r})$, as shown in Fig. 4, G to I.

Differing from transient vortex lines, which shrink with time owing to energetically costly cores and distorted order around them, vortex-meron knots in heliknotons are energetically favorable because they are nonsingular in the material $\boldsymbol{n}(\boldsymbol{r})$ field and comprise twisted structures with handedness matching that of the LC. The stability of our 3D topological solitons as spatially localized structures is assisted by the chiral term in Eq. 1, which introduces their finite dimensions and plays a role analogous to that of high-order nonlinear terms in solitonic models of subatomic particles (*3*–*6*) and the

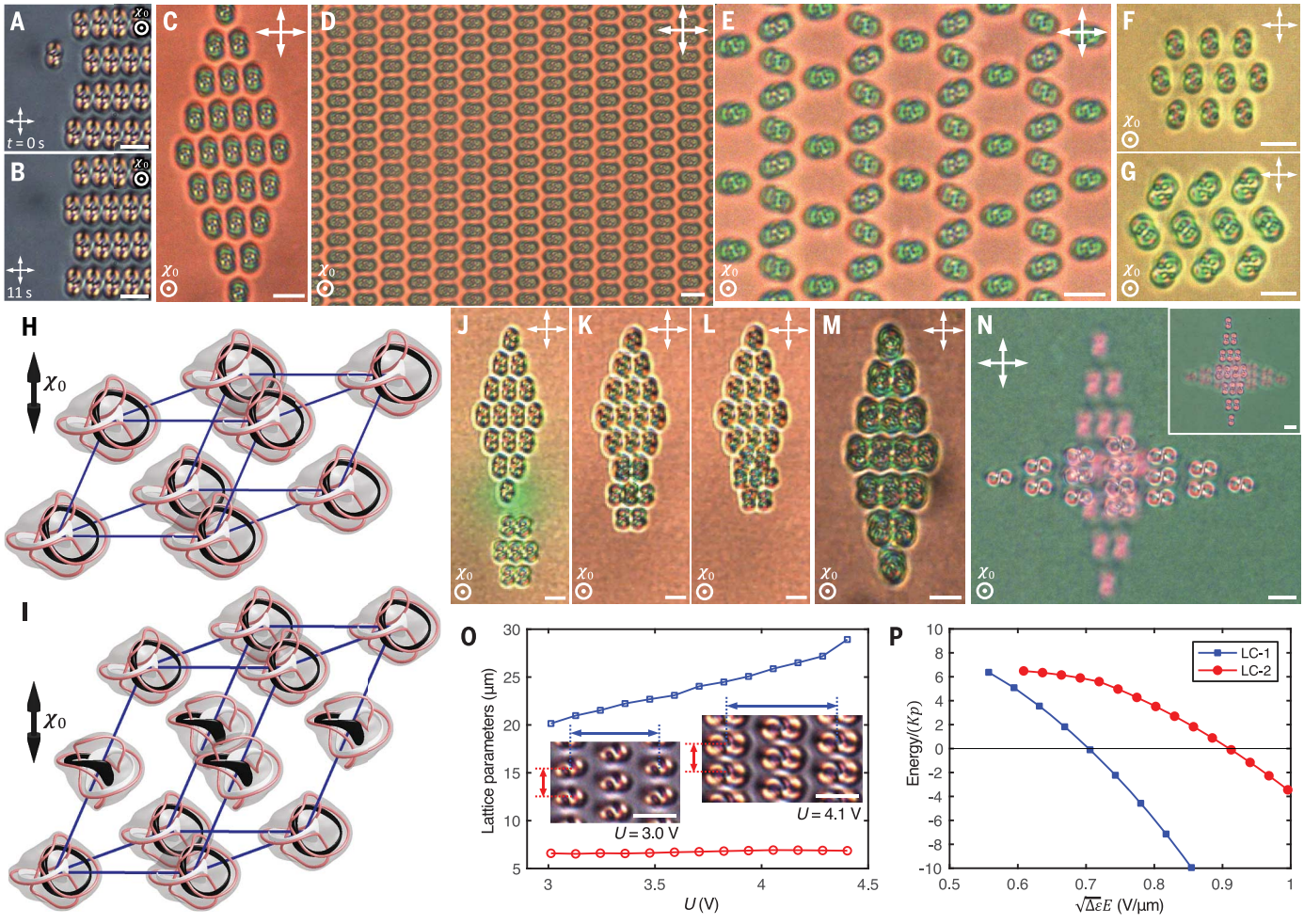

Fig. 2. Crystals of heliknotons. (**A** and **B**) Snapshots showing self-assembly of a 2D crystal ($d = 10$ μm, $U = 3.5$ V). (**C** to **E**) 2D closed rhombic [(C) and (D)] and open (E) lattices of heliknotons at $U = 1.9$ and 1.7 V, respectively ($d = 15$ μm). (**F** and **G**) Crystallites with aligned (F) and anticlinically tilted (G) heliknotons at $U = 1.8$ and 2.3 V, respectively ($d = 17.5$ μm). (**H** and **I**) Primitive cells of 3D heliknoton crystals where the solitons in neighboring horizontal layers have relative parallel (H) or perpendicular (I) orientations. Isosurfaces (gray) show the localized 3D regions of heliknotons with distorted helical background when colocated with both vortex knots (light red) and preimages of antiparallel vertical orientations in $\boldsymbol{n}(\boldsymbol{r})$ (black and white). (**J** to **L**) 3D interactions and self-assembly of heliknoton crystallites ($d \approx 30$ μm and $U = 2.8$ V). (**M** and **N**) 3D heliknoton lattices comprising crystallites with parallel (M) or perpendicular (N) orientations, where (N) and its inset are polarizing micrographs obtained when focusing at different crystalline planes ~10 μm apart ($d \approx 30$ μm in both cases and $U = 2.8$ and 3.4 V, respectively). (**O**) Electrostriction of a heliknoton crystal. Insets show lattices at different U, with the lattice parameters shown in blue and red ($d = 10$ μm). (**P**) Free energy of heliknoton crystals per primitive cell for two LCs at different $\boldsymbol{E}$. The heliknotons become metastable with respect to the unwound state at $\sqrt{\Delta\varepsilon}E \gtrsim 0.8$ V/μm for LC-1 and at $\sqrt{\Delta\varepsilon}E \gtrsim 1.2$ V/μm for LC-2. Data were obtained using LC-2 in (A), (B), and (O) and using LC-1 in (C) to (N) (*24*). Scale bars indicate 10 μm and $p = 5$ μm.

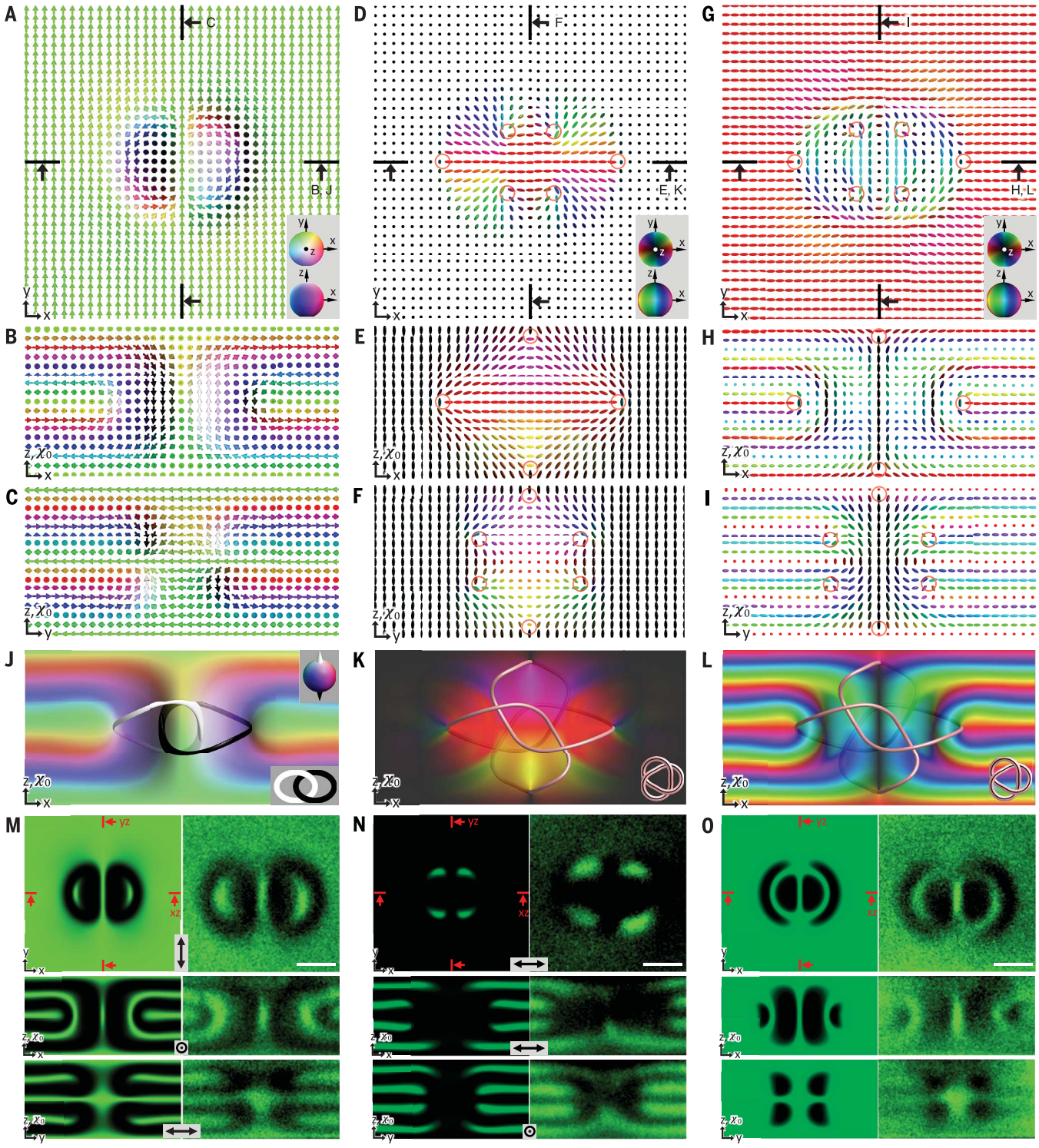

Fig. 3. Structure of an elementary heliknoton. (**A** to **I**) Computer-simulated cross-sections of $\boldsymbol{n}(\boldsymbol{r})$ [(A) to (C)], $\chi(\boldsymbol{r})$ [(D) to (F)], and $\tau(\boldsymbol{r})$ [(G) to (I)] of a heliknoton. Vertical cross-sections and the viewing directions are marked in (A), (D), and (G), respectively. $\boldsymbol{n}(\boldsymbol{r})$ is shown with arrows colored according to $\mathbb{S}^2$ [(A), inset], and $\chi(\boldsymbol{r})$ and $\tau(\boldsymbol{r})$ are shown with ellipsoids colored according to their orientations on the doubly colored $\mathbb{S}^2/\mathbb{Z}_2$ [(D) and (G), insets]. The vortex lines in $\chi(\boldsymbol{r})$ and $\tau(\boldsymbol{r})$ are marked by red circles in (D) to (I). (**J**) Preimages of vertical orientations of $\boldsymbol{n}(\boldsymbol{r})$ forming a Hopf link (bottom right inset) and the cross-section of $\boldsymbol{n}(\boldsymbol{r})$. (**K** and **L**) The singular vortex line in $\chi(\boldsymbol{r})$ and $\tau(\boldsymbol{r})$ forming a trefoil knot (bottom right insets) visualized by light-red tubes and the cross-sections of $\chi(\boldsymbol{r})$ and $\tau(\boldsymbol{r})$, respectively. (**M** to **O**) Computer-simulated and experimental nonlinear optical images of $\boldsymbol{n}(\boldsymbol{r})$ in the cross-sections of a heliknoton obtained with marked linear polarizations [(M) and (N)] and circular polarization [(O)]. Images on the left are numerical and those on the right are experimental, all obtained for LC-3 at $d = 10$ μm and $U = 1.7$ V (*24*). Scale bars indicate 5 μm and $p = 5$ μm.

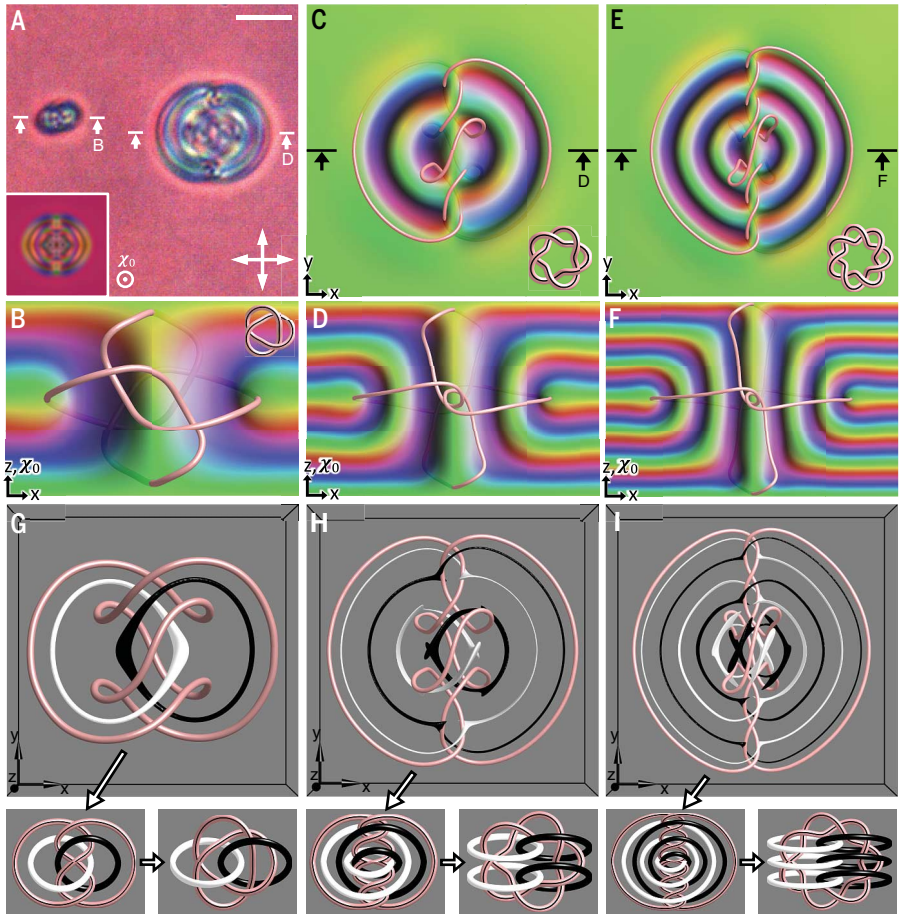

Fig. 4. Topologically distinct heliknotons. (**A**) Experimental polarizing optical micrograph showing an elementary $Q = 1$ (left) and a $Q = 2$ heliknoton (right), with the computer-simulated counterpart of a $Q = 2$ heliknoton shown in the inset ($d = 20$ μm; $U = 2.0$ V). (**B** to **F**) Midplane cross-sections colored by $\boldsymbol{n}(\boldsymbol{r})$ orientations on $\mathbb{S}^2$ and the knotted singular vortex lines in $\boldsymbol{\chi}(\boldsymbol{r})$ and $\boldsymbol{\tau}(\boldsymbol{r})$ shown as light-red tubes for $Q = 1$ [(B)], $Q = 2$ [(C) and (D)], and $Q = 3$ [(E) and (F)] heliknotons, respectively. The schematics of vortex lines forming right-handed T(3,2), T(5,2), and T(7,2) torus knots are shown in the insets of (B), (C), and (E), respectively. (**G** to **I**) Knotted preimages of vertical orientations in $\boldsymbol{n}(\boldsymbol{r})$ (black and white) and vortex lines in $\boldsymbol{\chi}(\boldsymbol{r})$ and $\boldsymbol{\tau}(\boldsymbol{r})$ (light red) for $Q = 1$, 2, and 3, respectively. Shown in the bottom parts of the panels are the sequences of Reidemeister moves transforming the energy-minimizing configurations into simplified links and torus knots. Scale bars indicate 10 μm and $p = 5$ μm; data were obtained for LC-1 (*24*).

Dzyaloshinskii–Moriya term in models of magnetic skyrmions (*13*, *14*). Applied field along $\boldsymbol{\chi}_0$ tends to reorient $\boldsymbol{n}(\boldsymbol{r})$ along $\boldsymbol{E}$ as compared to the helical state with $\boldsymbol{n}(\boldsymbol{r})\perp\boldsymbol{E}$. Consequently, the knots emerge as local or global energy minima within a certain range of voltages (*24*) by reducing the dielectric term in Eq. 1 compared with the helical state (Figs. 1H and 2P). At low $\boldsymbol{E}$, elastic energetic costs are high and heliknotons collapse into the helical background through spontaneous creation and annihilation of singular defects in $\boldsymbol{n}(\boldsymbol{r})$. The strong dielectric coupling between $\boldsymbol{n}(\boldsymbol{r})$ and $\boldsymbol{E}$ aligns $\boldsymbol{n}(\boldsymbol{r})||\boldsymbol{E}$ at high applied fields, eventually making both the helical structure and solitons unstable, but heliknotons are the global free-energy minima within broad, material-dependent ranges of $\boldsymbol{E}$ (*24*).

We have demonstrated 3D topological solitons in helical fields of chiral LCs that can be ground-state and metastable configurations, forming 3D crystalline lattices. Unlike the atomic, molecular, and colloidal crystals, heliknoton crystals exhibit giant electrostriction and marked symmetry transformations under voltage changes <1 V. We envisage that such solitons can emerge in helical phases of solid-state, noncentrosymmetric magnets (*13*, *14*, *22*) and ferromagnetic LCs (*23*) with helical fields and Hamiltonians similar to those of chiral LCs, where the roles of dielectric and chiral terms in Eq. 1 can be played by magnetocrystalline anisotropy and Dzyaloshinskii–Moriya interactions (*23*), respectively. Our crystals are experimental embodiments of matter made of Kelvin's vortex knots and Skyrme's knot solitons.

REFERENCES AND NOTES

1. X.-G. Wen, *Science* **363**, eaal3099 (2019).
2. L. H. Kauffman, *Knots and Physics* (World Scientific, 2001).
3. N. Manton, P. Sutcliffe, *Topological Solitons*. (Cambridge Univ. Press, 2004).
4. Y. M. Shnir, *Topological and Non-Topological Solitons in Scalar Field Theories*. (Cambridge Univ. Press, 2018).
5. T. H. R. Skyrme, *Proc. R. Soc. London Ser. A* **260**, 127–138 (1961).
6. L. Faddeev, A. J. Niemi, *Nature* **387**, 58–61 (1997).
7. H. K. Moffatt, R. L. Ricca, *Proc. R. Soc. London Ser. A* **439**, 411–429 (1992).
8. M. W. Scheeler, W. M. van Rees, H. Kedia, D. Kleckner, W. T. M. Irvine, *Science* **357**, 487–491 (2017).
9. D. Kleckner, W. T. Irvine, *Nat. Phys.* **9**, 253–258 (2013).
10. R. V. Buniy, J. Cantarella, T. W. Kephart, E. J. Rawdon, *Phys. Rev. D Part. Fields Gravit. Cosmol.* **89**, 054513 (2014).
11. R. Shankar, *J. Phys.* **38**, 1405–1412 (1977).
12. P. M. Chaikin, T. C. Lubensky, *Principles of Condensed Matter Physics* (Cambridge Univ. Press, 1995).
13. J. H. Han, *Skyrmions in Condensed Matter* (Springer, 2017).
14. D. Foster *et al.*, *Nat. Phys.* **15**, 655–659 (2019).
15. Y. Bouligand, *J. Phys.* **35**, 959–981 (1974).
16. Y. Bouligand, B. Derrida, V. Poénaru, Y. Pomeau, G. Toulouse, *J. Phys.* **39**, 863–867 (1978).
17. T. Machon, G. P. Alexander, *Phys. Rev. Lett.* **113**, 027801 (2014).
18. U. Tkalec, M. Ravnik, S. Čopar, S. Žumer, I. Muševič, *Science* **333**, 62–65 (2011).
19. A. Martinez *et al.*, *Nat. Mater.* **13**, 258–263 (2014).
20. D. Seč, S. Copar, S. Zumer, *Nat. Commun.* **5**, 3057 (2014).
21. P. J. Ackerman, I. I. Smalyukh, *Phys. Rev. X* **7**, 011006 (2017).
22. J.-S. B. Tai, I. I. Smalyukh, *Phys. Rev. Lett.* **121**, 187201 (2018).
23. P. J. Ackerman, I. I. Smalyukh, *Nat. Mater.* **16**, 426–432 (2017).
24. See materials and methods.
25. P. Poulin, H. Stark, T. C. Lubensky, D. A. Weitz, *Science* **275**, 1770–1773 (1997).
26. H. Mundoor, B. Senyuk, I. I. Smalyukh, *Science* **352**, 69–73 (2016).
27. V. N. Manoharan, *Science* **349**, 1253751 (2015).
28. X. Mao, T. C. Lubensky, *Annu. Rev. Condens. Matter Phys.* **9**, 413–433 (2018).
29. E. Efrati, W. T. Irvine, *Phys. Rev. X* **4**, 011003 (2014).
30. D. A. Beller *et al.*, *Phys. Rev. X* **4**, 031050 (2014).

ACKNOWLEDGMENTS

We thank P. Ackerman, M. Dennis, T. Lubensky, N. Manton, B. Senyuk, Y. Shnir, H. Sohn, R. Voinescu, and Y. Yuan for discussions. **Funding:** This work was supported by National Science Foundation grant DMR-1810513. **Author contributions:** J.-S.B.T. and I.I.S. performed research and wrote the manuscript. I.I.S. conceived the project and provided funding. **Competing interests:** The authors declare no competing interests. **Data and materials availability:** All experimental data are available in the main text or the supplementary materials.

SUPPLEMENTARY MATERIALS

science.sciencemag.org/content/365/6460/1449/suppl/DC1
Materials and Methods
Figs. S1 to S6
Table S1
References (*31*–*47*)
Data File S1
Movies S1 to S8

27 May 2019; accepted 16 August 2019
10.1126/science.aay1638